

Modelling the Galactic Magnetic Field on the Plane in 2D

T. R. Jaffe^{1*}, J. P. Leahy^{1†}, A. J. Banday^{2,3‡}, S. M. Leach^{4,5§},
S. R. Lowe^{1¶}, A. Wilkinson^{1||}

¹*Jodrell Bank Centre for Astrophysics, School of Physics and Astronomy, The University of Manchester, Oxford Road, Manchester, M13 9PL, United Kingdom*

²*Centre d'Etude Spatiale des Rayonnements, 9 av. du Colonel Roche, BP 44346, 31028 Toulouse Cedex 5, France*

³*Max Planck Institute for Astrophysics, Karl-Schwarzschild Str. 1, 85741 Garching, Germany*

⁴*SISSA, Astrophysics Sector, via Beirut 2-4, I-34014 Trieste, Italy.*

⁵*INFN, Sezione di Trieste, I-34014 Trieste, Italy.*

ABSTRACT

We present a method for parametric modelling of the physical components of the Galaxy’s magnetised interstellar medium, simulating the observables, and mapping out the likelihood space using a Markov Chain Monte-Carlo analysis. We then demonstrate it using total and polarised synchrotron emission data as well as rotation measures of extragalactic sources. With these three datasets, we define and study three components of the magnetic field: the large-scale coherent field, the small-scale isotropic random field, and the ordered field. In this first paper, we use only data along the Galactic plane and test a simple 2D logarithmic spiral model for the magnetic field that includes a compression and a shearing of the random component giving rise to an ordered component. We demonstrate with simulations that the method can indeed constrain multiple parameters yielding measures of, for example, the ratios of the magnetic field components. Though subject to uncertainties in thermal and cosmic ray electron densities and depending on our particular model parametrisation, our preliminary analysis shows that the coherent component is a small fraction of the total magnetic field and that an ordered component comparable in strength to the isotropic random component is required to explain the polarisation fraction of synchrotron emission. We outline further work to extend this type of analysis to study the magnetic spiral arm structure, the details of the turbulence as well as the 3D structure of the magnetic field.

Key words: ISM: magnetic fields – Galaxy: structure – polarisation – radiation mechanisms: general – radio continuum: ISM

1 INTRODUCTION

Observations of external galaxies show that the relationship between the magnetic field and the ionised gas is far from simple and varies from galaxy to galaxy. (See, e.g., Beck 2009 for a review.) Our own galaxy is more difficult to study since we must observe it from within and looking through the plane. In this work, we present a method for comparing magnetic field models of many parameters to a variety of observables. With the tools we describe, we can use more

realistic models for the small-scale components and therefore have less need for the simplifying assumptions (such as isotropy) that are often made with unknown effect on the results. For the first time, we now have coverage of significant portions of the Galactic plane in total and polarised synchrotron intensity as well as in rotation measures (RM), and we show how these complementary datasets are vital for disentangling the different components of the Galactic magnetic field.

It is useful to think of the Galactic magnetic field as separable into three components referred to as coherent, ordered, and random/tangled/turbulent. These are illustrated by the cartoon in Fig. 1. The term “coherent” refers to, e.g., a large-scale spiral structure, while the “random” component usually refers to the small-scale component varying in three dimensions in both strength and direction. The term “ordered” refers to a field where variations simply imply

* E-mail: tess.jaffe@manchester.ac.uk

† E-mail: j.p.leahy@manchester.ac.uk

‡ E-mail: Anthony.Banday@cesr.fr

§ E-mail: leach@sissa.it

¶ E-mail: Stuart.Lowe@manchester.ac.uk

|| E-mail: althea.wilkinson@manchester.ac.uk

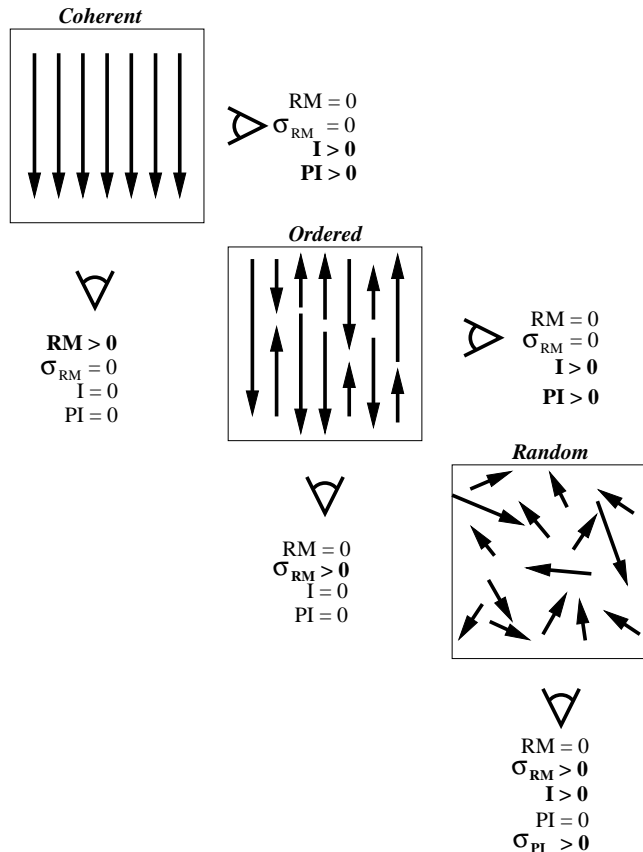


Figure 1. Cartoon illustrating the three components of the magnetic field and how they relate to the three observables of total synchrotron intensity (I), polarised synchrotron intensity (PI), and Faraday rotation measure (RM). **The variance of these is also of interest, as shown in the case of σ_{RM} .** (Note that the situation is the same for dust emission, which is also polarised perpendicular to the magnetic field due to grain alignment.)

sign reversals; the ordered component points along a common, ordered axis but simply changes direction on small scales, perhaps stochastically. (There are different uses of the word “ordered” in the literature. It can be thought of as an anisotropic random component, but in this paper, we will distinguish between an isotropic random component and an ordered component. “Ordered” is also sometimes used to refer to the combination of what we in this paper call the ordered plus coherent field, but we find that usage confusing and prefer to think of them as three distinct components.)

The coherent fields are assumed to probe processes such as galactic-scale dynamos, while the small-scale random component probes turbulent processes in the ISM. The ordered component is thought to result from the effects of larger scale shearing dynamics, compression, etc. on the random component. This component is often neglected for simplicity (see, e.g., Burn 1966).

In external galaxies, the synchrotron emission is compared to the thermal emission to study how the magnetic fields correlate with the ionised gas in the galaxy. The arms seen in total intensity tend to follow the arms seen in thermal emission, but the same is not true of the polarised intensity. This has two implications. Firstly, the random component is often significant, perhaps dominant, in the spiral arms, thus

lowering the polarisation fraction. Secondly, the ordered and coherent fields may be strongest in “magnetic arms” distinct from the spiral arms traced by the diffuse ionised gas (DIG) component. As reviewed by Beck (2009), NGC 6946 is an example where the magnetic arms appear to be between the arms traced by thermal emission, while M 51 appears to have magnetic arms on the edge of the spiral arms.

Though we cannot assume anything about how the magnetic field components correlate with the DIG, Fig. 2 shows that the synchrotron emission has clear step features that have been thought to correspond to arm tangents (e.g., Mills 1959 or Beuermann et al. 1985). The rotation measures also indicate field reversals that may be related. Learning how the field varies in strength, direction, and coherence across a spiral arm traced by diffuse gas will inform theories of how the fields are generated and maintained in the dynamic environment of the magnetised interstellar medium (MIM).

In this work, we take a first step toward disentangling these components in our own Galaxy. Since we cannot look down upon it from above to determine where the magnetic arms lie relative to the DIG spiral arms, we are limited to looking through the plane. Our ongoing project is to see whether the profiles in total and polarised synchrotron emission can distinguish arm ridges in the different components, but for this work, we assume that they all peak in the same ridges. We do not, however, constrain those ridges to lie where the DIG spiral arm ridges are thought to be, but instead use the data to constrain the orientation of the magnetic spiral arms. We leave it to later work to determine if the data can distinguish models where in addition to independent magnetic arms, the peaks in the three components do not coincide.

But there are several difficulties in interpreting the emission profile of synchrotron total intensity along the Galactic plane. Firstly, the random component introduces a sort of “galactic variance” (analogous in a limited sense to the cosmic variance in cosmic microwave background studies). Nearby random features will perturb the profile making it difficult to separate the field components accurately. Secondly, the plane contains a strong emission component from thermal bremsstrahlung, commonly known as free-free emission. This component is difficult to separate from the non-thermal emission we wish to study and has a different spatial distribution.

Using the polarised synchrotron emission in addition helps to resolve some of these problems, as the isotropic random component does not on average contribute to the polarised intensity. The addition of rotation measures further helps to break the degeneracies in the parameter space, as they are only dependent on the coherent component. The three field components can then be studied by comparing these three observables.

It is only recently that we have enough data to study the three components of the magnetic field and perhaps to separate them. We can look at the continuum emission and compare the total intensity to polarised intensity as well to the Faraday rotation measures. These three contain information about the relative strengths of the coherent, ordered, and random components. We now have synchrotron emission maps over the full sky at several bands including polarisation, and we have unprecedented coverage of a large part

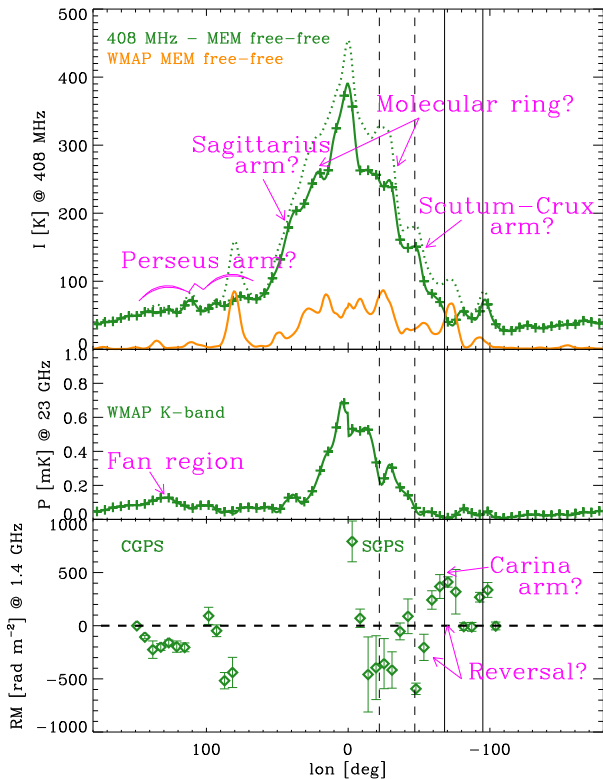


Figure 2. The three primary tools we use for studying the magnetic field in the plane of the galaxy are the synchrotron total intensity (*top*) from Haslam et al. (1982), the synchrotron polarised intensity (*middle*) from Hinshaw (2009), and the RM data (*bottom*) from Brown et al. (2003, 2007) averaged into roughly 6° bins. The field structures that we can perhaps infer from the profile of these data along the plane are indicated. The vertical lines mark interesting sight-lines (solid for positive RM, dashed for negative), also shown on Fig. 4, showing what may be tangents to arm features. Also shown in orange is the estimate for the free-free contamination which has been subtracted from the total emission at 408 MHz (dotted green line); see § 2.1.

of the Galactic plane in RMs of extragalactic sources. The combination of these datasets allows us to probe the three-dimensional distribution of magnetic fields and ionised gas in the Galaxy.

There has been much previous work to model the Galactic magnetic field, from Beuermann et al. (1985) and Broadbent et al. (1990) to Han et al. (2006), Page et al. (2007), Miville-Deschênes et al. (2008), Sun et al. (2008), Jansson et al. (2009), and Orlando et al. (2009). Most of these works use only one or two datasets and are limited by simplifying assumptions about the nature of the irregular components. Broadbent et al. (1990) (with more details in Broadbent 1989) consider a detailed galaxy model and have remarkable success in reproducing the profile of synchrotron emission along the plane. That work is unusual in including an analytic method to model the anisotropy in the small-scale random component of the MIM. While it seems unlikely that the data constrain all of the dozens of parameters in their model (particularly considering the

above-mentioned problems of thermal emission separation and galactic variance), we consider it an interesting place to start and adopt several aspects of their model. The more recent work of Sun et al. (2008) uses the three observables together to present a 3D model of the galaxy, but it does not explore the parameter space systematically and considers only what we define as the coherent and isotropic random magnetic field components. The work of Jansson et al. (2009) does a systematic search using MCMC, but they do not explicitly treat the random (or ordered) components and use only two of the three datasets we consider vital.

Our principle aim in this work is to describe a method to model the physical components of the MIM, to simulate the observables, and to map out the likelihood space using a Markov Chain Monte-Carlo (MCMC) analysis. The problem is a large and complicated one, and in this first paper, we focus on a 2-dimensional analysis on the Galactic plane only (seen as a 1D profile as in Fig. 2), though the methods can certainly be extended to model the Galaxy in 3D. We then demonstrate the method’s utility by using the available data to constrain the relative strengths of the three components of the magnetic field, the coherent, random, and ordered fields, and discuss how to extend the analysis using additional data.

2 OBSERVATIONS

2.1 Synchrotron emission in total intensity

The 408 MHz full-sky map by Haslam et al. (1982) primarily consists of synchrotron emission. (This map is available in HEALPix¹ format from the LAMBDA website².) The intensity gives information about the magnetic field (B) component perpendicular to the line of sight:

$$I_{\text{sync}}(\nu, p) \propto \int_{\text{LOS}} J_{\text{CRE}}(\mathbf{x}) B_{\perp}(\mathbf{x})^{\frac{p+1}{2}} dl \quad (1)$$

where I is the specific intensity and $J_{\text{CRE}}(\mathbf{x})$ is the density of cosmic ray electrons (CREs) described explicitly in § 3.5. The total intensity, or Stokes I , in a given observing beam is then $I = \int I d\Omega$.

The index on B depends on the spectral index, p , of the cosmic ray electron distribution, which we assume to be a power law. We follow the notation of Rybicki & Lightman (1979) and define the number density of particles in the range γ to $\gamma + d\gamma$ (where γ is the Lorentz factor such that $E = \gamma m_e c^2$) as $N(\gamma) d\gamma \propto \gamma^{-p} d\gamma$. Observations show that $p \approx 3$ between our two synchrotron observing frequencies of 408 MHz and 23 GHz (see, e.g., Finkbeiner 2004 or Miville-Deschênes et al. 2008), in which case $dI \propto B^2$. It also implies a power law in synchrotron flux density of $S \propto \nu^{-(p-1)/2} = \nu^{-1}$ or brightness temperature of $T \propto \nu^{-3}$. In reality, the spectral energy distribution of electrons will vary with position in the galaxy, but we will approximate it as a power law with a constant $p = 3$. The impact of this choice is discussed further in § 6.6.

The synchrotron total intensity is sensitive to all components of the magnetic field. The coherent component, random component, and ordered component all contribute according to their projection perpendicular to the line of sight.

¹ <http://healpix.jpl.nasa.gov/>

² <http://lambda.gsfc.nasa.gov/>

The profile of the synchrotron emission along the Galactic plane, shown in Fig. 2, has distinct steps, exactly as if the emission increases as the observer looks along a spiral arm. Unless this is coincidental, it therefore seems that either the magnetic field structure or the CRE density must follow to some degree the DIG spiral structure.

The 408 MHz map includes thermal bremsstrahlung (free-free) emission in a very narrow region about the Galactic plane. (Other available radio surveys include the 2.3 GHz data of Jonas et al. 1998 or the 1.4 GHz survey of Reich 1982 and Reich & Reich 1986. Higher frequencies, however, will have more free-free contamination due to its flatter spectral index.) Since it is along the plane that we are interested in the synchrotron emission, we must subtract the thermal emission. We use the Wilkinson Microwave Anisotropy Probe (*WMAP*) foreground maps generated from the maximum entropy method (MEM) described in Hinshaw et al. (2007). The *WMAP* MEM free-free map for the Ka-band (33 GHz) contains the best estimate of the free-free distribution that we have for the Galactic plane region. ((de Oliveira-Costa et al. 2008), for example, produce a synchrotron map using a combination of 11 different frequencies, but their principal components analysis results in the 408 MHz profile along the plane being virtually unchanged, indicating that the free-free component has not been subtracted.) The MEM maps are also available from the LAMBDA website.

The data are generated by starting with the full sky HEALPix maps at $N_{\text{side}} = 512$ (pixel size of 6.9 arcmin) for the Haslam and the *WMAP* Ka-band MEM free-free component. Each map is then smoothed to an effective beamwidth of 3° FWHM and the maps downgraded to $N_{\text{side}} = 128$ (pixel size of 27.5 arcmin). From the Haslam data, we then subtract the free-free component extrapolated from the Ka-band assuming a power law dependence of $\nu^{-2.1}$ (see, e.g., Dickinson et al. 2003). The 512-pixel ($4N_{\text{side}}$) slice along the plane is then extracted, further smoothed in 1-dimension by boxcar-averaging by 8 pixels, and the result is then downgraded to the 64 bins whose centres coincide with the $N_{\text{side}} = 16$ pixels along the plane. The result is a profile with a resolution of $\approx 6^\circ$ in longitude and three in latitude.

The reason for this processing is to minimize the effects of the inaccurate thermal emission separation. The *WMAP* MEM free-free component is generated by an analysis including only three foregrounds, namely synchrotron, free-free, and thermal dust. The results are therefore contaminated by the anomalous dust component. There is no other reliable indication of the thermal emission on the plane, however, ($\text{H}\alpha$, for example, is absorbed by dust on the plane and is only a reliable tracer of free-free at high latitudes) and the free-free emission is strong enough on the plane relative to the other components that the separation, while imperfect, is probably sufficient. The free-free latitude profile is very narrow (see e.g., Dickinson et al. 2003) compared to that of the synchrotron emission. Smoothing the maps first then leaves the profile of synchrotron emission along the plane essentially unchanged but reduces the relative amount of free-free emission.

In future work, we will investigate other ways to separate the thermal emission on the plane, for example by using the newer results from *WMAP* in Gold et al. (2009), which include a pixel-based MCMC separation method. In

that work, the authors estimate that the spinning dust fraction is at most $\approx 15 - 20$ per cent of the emission in the Ka-band. It is hard to predict the fraction that ends up in the free-free template (in either the MCMC or MEM analyses) when the spinning dust component is ignored, since this depends on whether its spectral behaviour better matches the free-free or the synchrotron. Note that the remaining uncertainties due to the inaccurate thermal emission separation and subtraction are unlikely to be as significant as the galactic variance described in § 1 itself.

Because the Galactic centre region is likely complicated and currently mysterious, we exclude the four nearest pixels corresponding to roughly 10° either side of $\ell = 0$. This makes the analysis insensitive to what happens in the innermost ~ 2 kpc of the galaxy and allows us to focus on the step-features as well as the general profile.

2.2 Polarised intensity

Polarised synchrotron emission depends on the cosmic ray power law spectral index, and is at most a fraction Π of the total intensity, where

$$\Pi \equiv \frac{PI}{I} = \frac{p+1}{p+7/3} = 0.75 \quad (2)$$

(for $p = 3$) in the case that the magnetic field is uniform (Rybicki & Lightman 1979). The observed degree of polarisation compared to the total intensity therefore gives information about how ordered the magnetic field is perpendicular to the line of sight. Averaging over an isotropic random component produces, on average, no polarised intensity, as emission polarised in perpendicular directions cancels. An *ordered* or anisotropic random component, however, will still add to the polarised intensity, since the polarisation angle depends only on the orientation rather than the direction of the field.

We use the Hinshaw (2009) five-year *WMAP* 23 GHz K-band map of polarised intensity and smooth it to extract the plane as described above for the Haslam data. Likewise, we ignore the four pixels toward the Galactic centre. This dataset is currently the best polarised synchrotron map in the high frequency regime where Faraday effects are negligible.

2.3 Faraday Rotation measure

The polarisation angle of an electromagnetic wave rotates when propagating through a magnetised plasma. The rotation angle changes as $RM\lambda^2$, where the Faraday rotation measure (RM) is defined as the the line-of-sight (LOS) integral from a source at a distance D :

$$RM \propto \int_D^0 n_e B_{\parallel} dl \quad (3)$$

where n_e is the number density of thermal electrons. A positive RM means that B_{\parallel} points toward the observer.

The RM can be measured for both pulsars within the galaxy as well as external sources. These data complement the synchrotron emission, since the RM is sensitive to direction as well as orientation and to the parallel component rather than the perpendicular. Therefore, averaged RMs trace only the coherent component of the magnetic field. If

the thermal electron density is uncorrelated with the magnetic field, then any random component or even ordered component will have a null effect on average, though it will naturally give rise to a variance in the manner of a random walk. This means that these data can help break degeneracies that arise in modelling the synchrotron emission due to the coherent versus random field parameters.

We are therefore probing three components of the magnetic field using three main datasets. There is a further source of uncertainty, however, namely the distribution of thermal electrons in the galaxy, discussed in § 3.4. As mentioned above, the relationship between the DIG and the magnetic field structure is unclear.

The data we use are the RMs for the extragalactic sources in the Canadian Galactic Plane Survey (CGPS) of Brown et al. (2003) and in the Southern Galactic Plane Survey (SGPS) of Brown et al. (2007). In the CGPS, there are a total of 380 sources within 5° of the plane in the range $82^\circ \leq \ell \leq 146^\circ$. In the SGPS, there are a total of 148 sources within 1.5° of the plane in the range $253^\circ \leq \ell \leq 356^\circ$. Following Brown et al., we exclude from our analysis the 30 sources in the region $270^\circ \lesssim \ell \lesssim 280^\circ$, where there is evidence for anomalously low RMs due to a local feature. To maintain consistency with the other datasets, we only use the 151 CGPS sources within 1.5° of the plane. That leaves a total of 269 sources used in our analysis covering a bit less than half of the Galactic plane. The sources are then averaged into the bins corresponding to those used for the other datasets.

There are additional RM data for galactic pulsars that may in future be added to our analysis. Because each pulsar is at a different LOS distance through the galaxy model, to include them would complicate the analysis and add considerable processing time. For this work, then, we use only extragalactic sources that give a full LOS through the galaxy.

3 GALAXY MODELS

We must model each of the relevant components of the MIM, namely the magnetic field (coherent, random, and ordered), the thermal electron spatial distribution, and the cosmic ray electron spatial and spectral distribution.

3.1 Coherent magnetic field

We model the coherent magnetic field beginning with a simple axisymmetric spiral that defines the direction of the field. In Sun-centric coordinates, then, the field direction is

$$\hat{\mathbf{B}} = \sin(\theta_p + \phi - \ell)\hat{\mathbf{x}} - \cos(\theta_p + \phi - \ell)\hat{\mathbf{y}}$$

where ϕ is the azimuthal angle in the polar coordinate system with the Sun at the origin, while ℓ is the Galactic longitude. We are working only in the plane, and the vertical component is always zero. (We use this form since we will integrate along the LOS from the Sun as the origin.)

This defines a spiral field with a pitch angle of $\theta_p = -11.5$. This angle is roughly that used in the thermal electron density model described in § 3.4. **Estimates of θ_p in the literature vary, however. Han & Qiao**

(1994) get $\theta_p = -8^\circ.2 \pm 0^\circ.5$ based on RM surveys, in rough agreement with the Heiles (1996) result based on starlight polarisation, $\theta_p = -7^\circ.2 \pm 4^\circ.1$. Miville-Deschênes et al. (2008) find a value of -8.5° based on WMAP polarised synchrotron emission, while Page et al. (2007) and Jansson et al. (2009) find best-fit pitch angles of as much as 35° . Jansson et al., however point out that this is highly model-dependent. In later work, we will allow this parameter to vary to see if it can be constrained better, and to investigate whether the magnetic spiral arms follow the matter spiral arms.

Broadbent et al. (1990) defined the coherent field amplitude as:

$$B(r) = B_0(1 - \exp(-r^2/R_2^2))(\exp(-r^2/R_0^2) + \exp(-r^4/R_1^4)) \quad (4)$$

where r is the Galacto-centric radius, and the three scale radii define the shape. Outside of the galactic centre region, this is a simple exponential drop as used in Han et al. (2006) to fit RM data or in Miville-Deschênes et al. (2008) for polarised emission. Because of its success predicting the synchrotron total intensity profile, even in the inner galaxy, in Broadbent et al. (1990), we start with this model. But we note firstly that Miville-Deschênes et al. (2008) find a constant amplitude fits the WMAP data better, and secondly, this profile is degenerate with the cosmic ray density profile described below in § 3.5. (In fact, Broadbent et al. use a constant CRE density, so their profile was essentially accounting for any radial variations in both components.)

Constraining this profile is beyond the scope of this paper, as it will require an additional observable such as dust emission to break the degeneracy. The default values we use are given in Table 1, though as described in § 2.1, we exclude the innermost longitudes from the analysis, which means the analysis is not sensitive to R_1 and R_2 . The value for R_0 is degenerate with the h_r parameter controlling the cosmic ray profile defined in § 3.5, also an exponential disc. The default values in Table 1 were set by eye to approximate the synchrotron profile so that we could explore the parameters determining the random versus ordered components. In a later paper, we will explore the radial profile parameters in more detail.

This azimuthally symmetric field is then amplified along spiral arm ridges (defined parallel to the field direction) as described in § 3.3. Note that those ridges are not constrained to lie along the DIG spiral arm ridges, and each magnetic arm has a corresponding amplitude parameter, a_n , so that we can fit for the strength of each arm independently. The parameters are summarised in Table 1 and the radial profile shown in Fig. 3.

3.2 Random magnetic field

The polarisation of synchrotron emission in the spiral arms of external galaxies is generally low (a few percent according to Beck 2009), implying that a large fraction of the total magnetic field is due to an isotropic random component.

The random component we simulate begins with a Gaussian Random Field (GRF) simulated in Fourier space (k is the wavenumber, $1/\lambda$) with a variance given by $|k|^{(\alpha-2)/2}$, where α is the spectral index of the power law de-

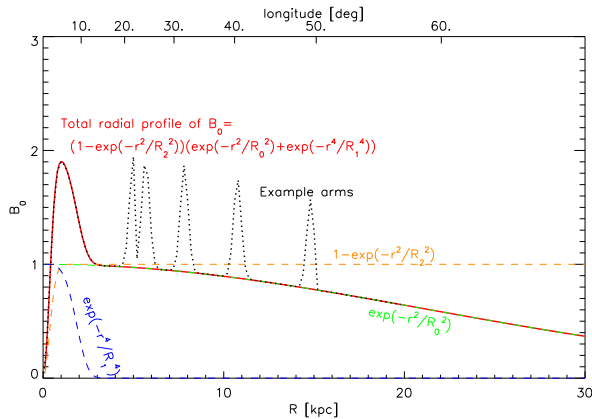


Figure 3. An example of the radial profile of the coherent field and of the compression. (Note that the values used are just for illustration and not those found to fit the data.) The uncompressed profile is shown in red, while the dotted black line includes the compression factor, $\rho_c(d)$, showing example spiral arms. The bottom axis is the radius from the Galactic centre, while the top axis is the corresponding longitude if viewed from the perpendicular direction at a distance of $R_{\oplus} = 8.5$ kpc.

describing the total magnetic energy in one dimension, $P(k) \propto k^\alpha$, following Han et al. (2004). For a Kolmogorov-type simulation that perhaps matches the small-scale ($1/k \lesssim 1$ pc) fluctuations, $\alpha = -5/3$, while Han et al. (2004) find an index of $\alpha = -0.37$ at larger ($1/k \gtrsim 1$ kpc) scales.

This field in k -space is then Fourier transformed to real space and amplified along the ridges of magnetic spiral arms by a parametrized compression described in the next section.

In this paper, we are simulating the entire galaxy, though only in two dimensions. In § 5, we describe how the resolution of the random component affects the results. In short, we find that the analysis of the whole plane at low resolution is not strongly sensitive to many parameters of the GRF. We use the spectral index for larger scales, $\alpha = -0.37$, a box size 40 kpc long on each side, and 512 bins for a bin size of 80 pc. This is very low resolution and not much better than a single scale random component. But as described in § 5, we find that increasing the resolution does not change the results significantly.

For later papers, we will analyse small regions of the sky at high resolution (e.g., pixels of 0.5 arcmin) and look in detail at the properties of the turbulent component, but for this paper, those details are not constrained.

3.3 Compression

As discussed above, in some external galaxies, the magnetic field appears enhanced in the spiral arms as traced by the DIG, while in others, there appear to be separate “magnetic arms”, sometimes between the DIG arms or showing a different (even varying) pitch angle. We therefore define a logarithmic spiral arm model for such ridges parallel to the coherent field direction and allow the orientation of the spiral to vary to fit the data. In addition to the spiral arms, we also include an annulus at 5 kpc from the Galactic centre,

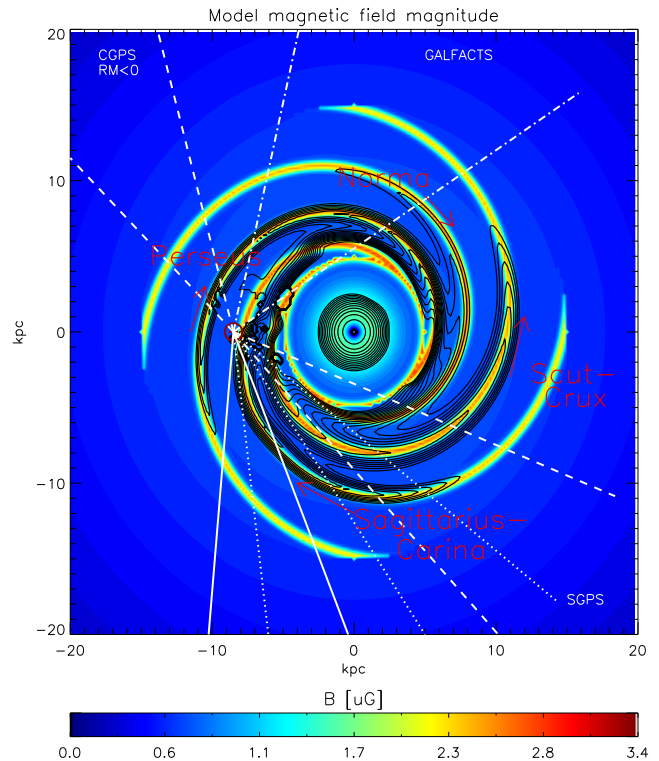


Figure 4. An example of a coherent spiral arm magnetic field model (no random component shown) compared to NE2001 spiral model for the thermal electron density shown as overlaid contours. Interesting sight-lines are over-plotted corresponding to the vertical lines in Fig. 2. The peaks in the RMs correspond to looking roughly tangentially to a spiral arm. (Note that the contours do not make clear the high-density “molecular ring” between roughly 2 and 5 kpc of the Galactic centre.) For comparison with Table 1, the Perseus arm corresponds to amplitude a_0 , Sag-Carina with a_1 , Scut-Crux a_2 , Norma a_3 , and the ring a_4 . (As discussed in § 3.1, the parameters used in this example are *not* necessarily the defaults in that table.)

roughly coinciding with the “molecular ring” feature in the NE2001 model.

We define a four-arm model in this paper, and will test other models in a later work. Each arm is then described by a curve

$$r(\phi) = R_s \exp[(\phi_{0n} - \phi)/\beta] \quad (5)$$

where $\beta \equiv 1/\tan(\theta_p)$, θ_p being the same pitch angle defined above for the coherent field direction. The angle ϕ_{0n} is the reference angle for the n^{th} spiral arm, always $\pi/2$ away from its neighbours in the case of four arms.

The arm ridges (and ring) are then defined by a modulation that peaks along the ridge and reaches a minimum between the arms. The compression profile we use is based on Broadbent et al. (1990), who modelled a magnetic field component that is enhanced in the arm by a compression factor ρ_c ,

$$\rho_c = C_0 \exp(-(d/d_0)^2) + 1 \quad (6)$$

where d is the distance to the nearest of the four arm ridges as measured along the line passing through the Galactic centre.

This implies a field that is unaltered between the arms

but amplified in the arms according to a Gaussian profile, when seen through a radial cross-section, with a width of d_0 . This amplitude enhancement profile applies to both the isotropic random component and the coherent component. This Gaussian modulation may not accurately represent what may in reality be a shock front with a different profile, but it is meant simply as a first order approximation to an enhancement parallel to the shock plane. (Though we refer to the “shock plane”, note that ρ_c is not the density contrast across the shock, as often used, but simply the total Gaussian density enhancement as compared to the unshocked inter-arm region.) An example of the compressed coherent field viewed from above is shown in Fig. 4.

To simulate an ordered component, the random field is then also *stretched* along the plane defined by the arm ridge. This can be thought of as an anisotropic random component, or as the addition of an ordered component (in addition to the coherent and isotropic random components) whose orientation is always along the spiral arm but whose specific direction changes stochastically. Rather than using the numerical approximation given in Broadbent et al., we apply this compression explicitly to our simulated random component. Namely, we use

$$\mathbf{B}_{\text{irreg}} = \rho_c \mathbf{B}_{\text{GRF}} + f_{\text{ord}}(\rho_c - 1) \mathbf{B}_{\text{GRF}}^{\text{proj}} \equiv \mathbf{B}_{\text{iso}} + \mathbf{B}_{\text{ord}} \quad (7)$$

where $\mathbf{B}_{\text{GRF}}^{\text{proj}}$ is the component of the random field projected onto the shock plane,

$$\mathbf{B}_{\text{GRF}}^{\text{proj}} = \mathbf{B}_{\text{coh}} \frac{\mathbf{B}_{\text{coh}} \cdot \mathbf{B}_{\text{GRF}}}{|\mathbf{B}_{\text{coh}}|^2}, \quad (8)$$

and f_{ord} sets the ratio of the ordered field to the amplified but isotropic random component in the arms. (Note that f_{ord} is not the ratio itself, since that changes from the arm to inter-arm regions.) The first term in Eq. 7 is then the isotropic (but no longer homogeneous) random component while the second term is the ordered component. The shock plane is assumed to be perpendicular to the Galactic plane and parallel to the spiral arm traced by the coherent component.

The form of this parametrization means that in the inter-arm regions, the ordered component goes to zero, while the isotropic random component is not amplified but non-zero. The combination of B_{RMS} and C_0 determines the amplification in the arm relative to the inter-arm region. In particular:

$$\langle B_{\text{iso}}^2 \rangle^{1/2} = \begin{cases} \langle B_{\text{GRF}}^2 \rangle^{1/2} \equiv B_{\text{RMS}}, & \text{as } \rho_c \rightarrow 1 \text{ (interarm)} \\ (C_0 + 1) B_{\text{RMS}}, & \text{as } \rho_c \rightarrow C_0 + 1 \text{ (ridge)}. \end{cases} \quad (9)$$

In other words, in the inter-arm region, d is large, ρ_c goes to 1 (see Eq. 6). On the ridge, d goes to zero, ρ_c reaches its maximum at $C_0 + 1$, and the random component is amplified by $C_0 + 1$. In between, the amplification is falling off with a Gaussian profile of width d_0 . The profile of the ordered component, proportional to $\rho_c - 1$, is the same Gaussian but without the offset, i.e., it goes to zero between the arms:

$$\langle B_{\text{ord}}^2 \rangle^{1/2} = \begin{cases} 0, & \text{as } \rho_c \rightarrow 1 \text{ (interarm)} \\ f_{\text{ord}} C_0 \langle (B_{\text{GRF}}^{\text{proj}})^2 \rangle^{1/2}, & \text{as } \rho_c \rightarrow C_0 + 1 \text{ (ridge)} \end{cases} \quad (10)$$

Note that this model approximates the case where the ordered component is due to the compression wave in the arm, but it does not represent the possibility that the ordered component might arise simply due to differential rotation.

The ratio of ordered to random is then zero in the inter-arm regions; along the ridge, the ratio is

$$\frac{\langle B_{\text{ord}}^2 \rangle^{1/2}}{\langle B_{\text{iso}}^2 \rangle^{1/2}} = f_{\text{ord}} \frac{C_0}{C_0 + 1} \sqrt{\frac{2}{3}} \quad (11)$$

because $\langle (B_{\text{GRF}}^{\text{proj}})^2 \rangle = 2/3 \langle B_{\text{GRF}}^2 \rangle$.

When looking down a spiral arm, the ordered component does not contribute to the synchrotron emission. The impact of this change on total intensity is then seen in the *relative* amount of emission seen looking down an arm relative to elsewhere, i.e., in the shape the emission steps seen in the longitude profiles in Fig. 2. Since the isotropic component does not contribute to polarisation, the ordered component, along with the coherent field, also determines the polarised emission profile.

The same effect on the synchrotron can be obtained with an isotropic compression of the random component combined with a stronger coherent component. Amplifying the random component along the arms essentially adds an ordered component, which as described above, is indistinguishable from a coherent component in synchrotron. The two cases can be distinguished, however, by looking at the rotation measures as well, where a too-large coherent component will overpredict RM.

3.4 Thermal electrons

For the thermal electrons, we consider three possibilities:

- a physically unrealistic constant density;
- the NE2001 model; or
- a parametrized spiral arm structure analogous to the coherent magnetic field component.

The thermal electron density model that has been most widely used is that of Cordes & Lazio (2002), known as NE2001. Based on observations of pulsars at known distances, this model relates the thermal electron density, n_e , to the dispersion measure (DM) of a give source and its distance, D :

$$DM \equiv \int_0^D n_e dl \quad (12)$$

Though this model was intended for determining pulsar distances, it is also used for modelling the magnetic field through RM, as it is the best existing predictor of the thermal electron density.

The constant model is useful as a comparison to determine whether or not we can distinguish either of the others from the null hypothesis. We have compared the results of using a constant density to those using the NE2001 model and find that the resulting data profiles are largely indistinguishable. The models and RM data are shown in Fig. 5, with the corresponding parameters that were fitted listed in Table 2. (The synchrotron profiles, not shown, are effectively indistinguishable.) The curves are essentially the same, and though the individual arm amplitudes change, the effect on

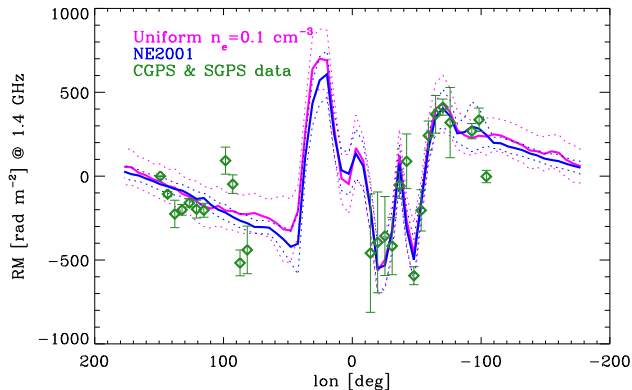


Figure 5. A comparison of the rotation measures from two models fitted to the CGPS and SGPS data, in the one case with a constant thermal electron density of $n_e = 0.1$ and in the other case with the NE2001 prediction. The best-fit parameters are given in Table 2. (The dotted lines indicate the galactic variance due to the random magnetic field component.)

the synchrotron emission would be very difficult to distinguish.

In this work, we use the NE2001 thermal electron density model unless otherwise specified. Though it is not likely to be correct in detail, it is at least based on observations and provides the best current estimate.

The possibility of defining our own model introduces quite a few more parameters to the problem, and those are unlikely to be constrained with the data we are using. In the future, however, we can include dispersion measures that depend only on the thermal electron density (and are calculated in the integration code we use) and additional data about the distribution from H α emission. The tools we use can be extended to include galactic pulsars, comparing that additional RM and DM data to better map out the thermal electron distribution near the Sun. As each pulsar is at a different distance, this complicates the LOS integration and the likelihood exploration, but in future work, we can explore this idea further.

3.5 Cosmic-ray electrons

The spatial and spectral distribution of cosmic rays in the Galaxy is thought to be fairly smooth until energies above 100 GeV (see, e.g., Strong et al. 2004 and Strong et al. 2007). But it is not clear *how* smooth the distribution is, and local measurements are obviously affected by local sources, so it is difficult to determine the average distribution over the galaxy.

For the purposes of constraining the structure of the magnetic field, however, we start simple. We adopt an exponential disc model such as that used by Page et al. (2007) and Sun et al. (2008) (motivated by the work of Drimmel & Spergel 2001), namely

$$J_{\text{CRE}}(r, z) = J_{\text{CRE},\oplus} \exp(-(r - R_{\oplus})/h_r) \quad (13)$$

where R_{\oplus} is the Galactocentric radius of the Solar system. (In the current analysis on the plane only, we neglect any modulation with height.) The normalisation is uncertain,

but as a first estimate, we read off the value at 10 GeV from Fig. 4 of Strong et al. (2007) of roughly $E^3 J(E = 10 \text{ GeV}) \approx 250 \text{ GeV}^2 \text{ m}^{-2} \text{ s}^{-1} \text{ sr}^{-1}$. We then use the value of $J_{\text{CRE},\oplus} = 0.25 (\text{GeV m}^2 \text{ sr})^{-1}$ to set the cosmic ray normalisation.³ For comparison, Sun et al. (2008) use a value of $J_{\text{CRE},\oplus} = 0.4 (\text{GeV m}^2 \text{ sr})^{-1}$.

For this work, we also adopt a simple power law energy distribution with the index $p = 3$.

We should emphasize that this model is overly simplistic in assuming a smooth spatial distribution and a simple power law spectrum that is the same throughout the Galaxy. Neither of these assumptions is likely to be true in reality. What we are constraining is then the spatial distribution of the product $n_{\text{CRE}} B^2$. The degeneracy between spatial variations in the two independently is only broken for the coherent field using the rotation measure data. In a later work, we will see how much the two can be separated by adding thermal emission from dust to the analysis.

4 MODEL SELECTION METHOD

The problem is then to parametrize the Galactic magnetic field (as well as the thermal and cosmic ray electrons if possible) and find the model parameters that best fit the data. There are, then, a large number of parameters, and a brute-force approach like a simple grid search would require prohibitive amounts of computing time. Instead, we use the far more efficient and flexible method of a Monte Carlo Markov Chain (MCMC) analysis.

4.1 Simulation with HAMMURABI

The likelihood function we use computes a simple χ^2 from a comparison of the model to the data along the Galactic plane as shown in Fig. 2. For the given values of the input parameters, we generate the observed emission and RM at each pixel by performing a line-of-sight integration through a simulated galaxy using the HAMMURABI code of Waelkens et al. (2009).

The HAMMURABI code is designed to compute observables such as synchrotron emission and dust emission in full Stokes parameters while taking into account Faraday rotation and depolarisation effects. It performs a line-of-sight integration through a galaxy simulation, but uniquely, it can refine the integration resolution as the distance increases in order to maintain a roughly constant physical cell size. This is crucial for simulating effects such as beam depolarisation. We do not take full advantage of this code in this current work, but we will later use it to investigate more thoroughly the properties of the turbulent ISM and its effect on the observables.

For this analysis, we simply use one observing “shell”

³ This is sometimes expressed as a spatial number density normalisation. The spatial number density (assuming relativistic electrons with $v \sim c$) is then $N(E) = J(E) \times 4\pi \times 1/c$. Often, what is given is a normalisation $C(r, z)$ such that $N(\gamma)d\gamma \equiv C(r, z)\gamma^{-p}d\gamma$ where γ is the Lorentz factor ($E \equiv \gamma m_e c^2$). Therefore, $C_{\oplus} = N(\gamma)\gamma^p = J \times \frac{4\pi}{c} \times m_e c^2 \times \left(\frac{10 \text{ GeV}}{m_e c^2}\right)^3 = 4 \times 10^{-5} \text{ cm}^{-3}$, assuming $p = 3$.

Parameter	Default	Equation	Description
Coherent magnetic field: $B_{coh}(r, \phi) = B_0(r)a_n\rho_c(d)$			
B_0	1 μG		Global amplitude normalisation
R_s	7.1 kpc	see p	Scale radius of spiral.
θ_p	-11.5	$\beta \equiv 1/\tan(\theta_p)$ and $r(\phi) = R_s \exp[(\phi_0 - \phi)/\beta]$	θ_p is the pitch angle of spiral ($r(\phi)$ gives arm radius at given azimuth)
ϕ_0		See pitch	Angle representing rotation of spiral around axis through Galactic poles
R_{mol}	5. kpc		Radius of ‘‘molecular ring’’
R_{max}	20 kpc		Maximum radius, beyond which $ B = 0$
$R_{\text{max}}^{\text{arms}}$	15 kpc	See C_0	Maximum radius, beyond which $C_0 = 0$ (see C_0).
N_{arms}	4		Number of spiral arms
a_n		$B_{coh}(r, \phi) = B_0(r)a_n\rho_c(d(r, \phi))$	Amplitude modulation and direction for a given arm, n .
d_0	0.3 kpc	$\rho_c(d) = C_0 \exp(-(d/d_0)^2) + 1$	Defines width of arm for density enhancement, ρ_c ; d is the distance to the nearest arm in kpc
R_0	20 kpc	$B_0(r) = B_0(1 - \exp(-r^2/R_0^2))(\exp(-r^2/R_0^2) + \exp(-r^4/R_1^4))$	Outer radial profile parameter. See Fig. 3.
R_1	3 kpc	see R_0	Inner radial profile parameter
R_2	0.5 kpc	see R_0	
C_0	1	See d_0 . $C_0 = 0$ if $r > R_{\text{max}}^{\text{arms}}$	Peak density contrast. Sometimes $C_0 \propto a_n$; see § 6.4.
Random and ordered magnetic field			
α	-0.37	$P_B(k) \equiv \langle B_{\text{ran}}(k)^2 \rangle \propto k^\alpha$	Power law spectral index of initial GRF; default from Han et al. (2004) in 1D, Kolmogorov value $-5/3$.
D_{co}	1 kpc	$B_{\text{ran}}(k) = 0$ for $k < 1/D_{\text{co}}$	Cutoff maximum of GRF fluctuations (minimum determined by resolution)
B_{rms}		$B_{\text{rms}} \equiv \langle B_{\text{ran}}^2(\mathbf{x}) \rangle^{1/2}$	Total RMS amplitude of GRF fluctuations
f_{ord}		$\mathbf{B}'_{\text{ran}} = \rho_c \mathbf{B}_{\text{ran}} + f_{\text{ord}}(\rho_c - 1)\mathbf{B}_{\text{proj}} \equiv \mathbf{B}_{\text{iso}} + \mathbf{B}_{\text{ord}}$	Relates ordered to isotropic random component
Thermal electrons			
n_{e0}	-	$n_e(r, \phi) = n_{e0}$	Alternative constant density test model. By default, we use the NE2001 model of Cordes & Lazio (2002), which peaks in the arms around 0.1 cm^{-3} .
Cosmic-ray electrons			
p	3		Electron power spectrum power law index. See § 2.1 and § 3.5.
h_r	15 kpc	$J_{\text{CRE}}(r) = J_{\text{CRE},\oplus} \exp(-(r - R_{\oplus})/h_r)$	Scale radius of CREs.
$J_{\text{CRE},\oplus}$	$\frac{0.25}{\text{GeV m}^2 \text{ s sr}}$		See § 3.5.

Table 1. Table of modelling parameters as described in § 3.

(i.e., no grid refinement with distance) and a simple 2D simulation in the plane of the Galaxy only. We compute the observables at each of 512 pixels along the plane that correspond to the centres of the HEALPix pixels on the plane in a map at $N_{\text{side}} = 128$ map. We then smooth the result in the same way we smoothed the data as described in § 2.1 and bin them into 64 pixels.

4.2 MCMC with COSMOMC

For the MCMC sampling, we use the tools already developed by Lewis & Bridle (2002) and publicly available as the package COSMOMC. It consists of a Fortran sampling routine, into which one can insert a parametrized likelihood function, and

an analysis tool, *getdist*, to read the resulting Markov chains and determine the parameters’ mean and maximum likelihood values and correlation matrices. We use the COSMOMC sampler but have written our own analysis tool in order to add further functionality described below. The sampler has the ability to continuously update the proposal density based on the likelihood space so far sampled, which makes for a more efficient mapping out of the likelihood.

This method is complicated in this case by the fact that we do not compute the model, i.e., the simulated emission and rotation measures, analytically. Rather, as described above, we simulate a Gaussian random field for the random component and apply the compression algorithm. The model we wish to compare to the data is then the expecta-

tion value of the emission profiles resulting from such simulations, and the corresponding variance among realisations determines the error. These are difficult to compute analytically, so we instead use a brute-force approach of creating a set of $N = 10$ realisations and taking the mean. This must be done for each likelihood evaluation. (We have tried several different numbers of realisations at each sample and found ten to be the most efficient in terms of the trade-off between sample variance and run time.)

For simplicity, we assume a Gaussian distribution of the data points, x_i , about the mean model value, μ_i , with a variance of σ_i so that the likelihood is:

$$-\ln(\mathcal{L}) = \sum_i \ln(\sqrt{2\pi}\sigma_i) + (x_i - \mu_i)^2 / (2\sigma_i^2) \quad (14)$$

(where the summation is over the pixels along the plane). The distributions are not exactly Gaussian, as can be seen in Fig. 6, but the assumption appears to work reasonably well nonetheless. The differences come from the relation between the Gaussian random field and the observables, which in the case of the synchrotron emission, is non-linear. The RMs of extragalactic sources start with an average value through the galaxy, dependent only on the coherent component of the magnetic field, that is then perturbed by a one-dimensional random walk due to the random magnetic field component projected along the LOS (assuming the small-scale fluctuations are uncorrelated with the thermal electrons). The random component then adds a variance proportional to the number of steps. (Because the random component has structure on many scale lengths, it is essentially a superposition of random walks with different sized steps.) For polarised intensity, the polarisation vector behaves like a two-dimensional random walk, and the observable is only the length of the result. With only a GRF, the expectation value of either Stokes Q or U would be zero, but the expectation of $P = \sqrt{Q^2 + U^2}$ is non-zero and adds to the coherent component. For total intensity, the emission of all components simply adds.

Note that the variance at each longitude depends both on the position and on the model parameters and is determined simply from the variance of the simulated realisations. There is an additional uncertainty in both the model mean, μ_i , and its variance, σ_i , due to the limited number of realisations, so in the determination of χ^2 , we actually use

$$\hat{\sigma}_i^2 = (1 + 1/N)\sigma_i^2 \quad (15)$$

in the likelihood evaluation of Eq. 14.

When analysing the chains, there is essentially an additional “noise” term added to the likelihood space, since two evaluations at the same point in parameter space will return slightly different likelihoods. This means that we need more samples to overcome the sample variance and to map accurately the shape of the likelihood space. It also means that we need to give a “temperature” parameter to the sampler. The latter is necessary to prevent the algorithm from falling into an unusually low χ^2 hole and never getting out again. So rather than sampling from $P \propto \exp(-\chi^2/2)$, we sample from $P \propto \exp(-\chi^2/2T)$, where T is not a physical temperature but simply a way to adjust the sampler. This temperature is simply tuned to ensure that the acceptance rate of the sampler (i.e., the fraction of proposed samples that are accepted) remains roughly a third. (With a total

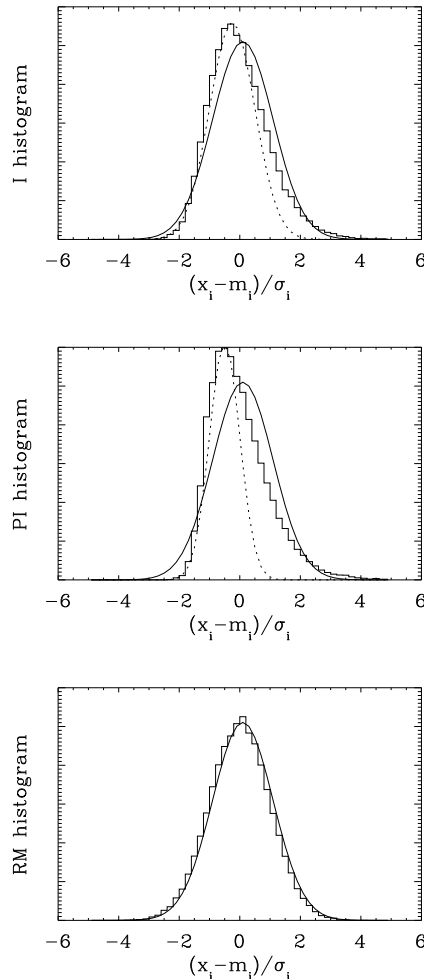


Figure 6. Distribution of data values compared to the mean. For 1000 simulations and 64 pixels along the plane, the histogram shows the difference between the data for a given simulation and at a given pixel, x_i , and the mean at that pixel over all simulations, m_i , normalised by the variance, σ_i . Clearly, for total and polarised intensity, there is a tail on the positive side that biases the mean. The solid line shows a Gaussian of the equivalent mean and width, which is essentially what using a χ^2 assumes, while the dotted line shows a Gaussian that approximately fits the left half of the histogram.

of 140 data points and corresponding χ^2 values, we find a temperature of 10 usually sufficient.) This temperature correction is then reversed to analyse the results, correcting both the likelihoods as well as the weights (the number of steps in the chain where it remained at a given sample before it accepted the next).

To simplify the analysis of the chains, we need to remove this noise, and we do this simply by smoothing the likelihood space (as, for example, done in Dick et al. 2006). For each sample, we replace the likelihood with the mean of the nearby likelihoods. We must also smooth the weights, which are by construction meant to be proportional to the likelihood. The result of the smoothing is a distribution of likelihood values approximating that seen in an essentially noiseless situation with otherwise identical parameters. We

smooth by binning the samples in likelihood space with a binsize of 1/15 times the range (after burn-in) for each parameter.

The number of samples required for the chains to converge (using COSMOMC's parameter `MPI_Limit_Converge_Err = 0.3`) is between a few thousand for a 2D fit and a few hundred thousand for a 6D fit.

In §5, we describe how we tested with simulated inputs to verify that the MCMC search returns the input parameters and reasonable uncertainties. An example is shown in Fig. 7.

4.3 Parameters and datasets

One could, in theory, throw all data and all parameters into the MCMC analysis at once, but it would be surprising if such an approach yielded useful information. Degeneracies among parameters make samplers highly inefficient, and when starting values are very far from the peak likelihood, the burn-in time to random-walk over to the peak can be very long. Instead, we make educated guesses (informed by trial and error) about what combinations of parameters and data will give good constraints and test them using simulations. For the parameters we fix for the course of the analysis, we choose by hand values that roughly match the data, since these are not our primary interest.

For example, as described above, the RMs are the best dataset to constrain the coherent magnetic field component. Particularly, the angle ϕ_0 describing the azimuthal orientation of the spiral may have a strong effect on the position of the RM sign reversals, while the a_n describe the relative magnitudes of the RM features. While these parameters do have an effect on the profiles of the synchrotron emission, given the galactic variance, this may not be detectable. So to determine these parameters, then, we use only the RM data.

The synchrotron emission is particularly interesting for studying the different components of the random field. As described above, we can use the RMs to constrain the coherent field and then use the synchrotron to constrain the parameters such as B_{rms} and f_{ord} , keeping ϕ_0 and a_n fixed to their best-fit values from the RM-only analysis.

Table 1 lists all of the parameters that go into the modelling, and clearly studying all of them would be a huge undertaking. For this first paper, we focus on the most immediately interesting issues of the magnetic field reversals and the relative contribution of the coherent, ordered, and random components.

5 TESTING

5.1 Basic Parameters

Figure 7 shows an example of how the MCMC method works with a simulated dataset. The results on the left use only RM data covering roughly half of the plane. Among the six parameters simultaneously fit for this test (all a_n and ϕ_0), all return a mean, μ_i , that is within 2σ of the input value, μ_0 , where σ is the variance of the samples.

On the right of Fig.7 is the result of the second step of fitting. We fix the amplitudes at the values found using the

RM data only and then fit to all data the two parameters controlling the ratio of ordered to random magnetic fields in the arms. The returned values lie roughly within 1σ of the correct values.

We have run a set of ten such simulations to verify that the estimates of f_{ord} and B_{RMS} are correct and unbiased (i.e., $|\langle\mu_i\rangle - \mu_0| < \sigma/\sqrt{10}$).

5.2 Resolution

Figure 8 shows a test of the importance of the resolution level in the simulations along the plane. Here, we test the implications of the simplifications we make for computational efficiency.

The choice of the resolution of the GRF simulation is an important question. The GRF normalisation, e.g., its RMS over the whole galaxy box, is a function of the outer scale, the power law index, and the resolution. Though the smaller scales are increasingly irrelevant due to the power law's negative spectral index, there is an effect of not including all relevant dynamical scales. We have verified that quadrupling the resolution appears to have only a small effect on the results of the simple Galactic plane analysis, as seen in Fig. 8.

More importantly, we simulate only a 2-dimensional GRF rather than a full 3-D galaxy, which speeds up the computation by almost a factor of ten. Though we are only looking along the Galactic plane, structure near the plane does enter the beam of each observation, particularly for volumes further away. To be fully correct, we would simulate a 3D galaxy and include contributions from high-resolution pixels just off the plane by using multiple HAMMURABI shells to simulate a finite instrument beam. The differences in the profiles are shown in Fig. 8. There is a visible difference in the total intensity profiles; the blue curve shows the correct profile, while the red is what we simulate. The effect of this simplification is to underestimate the RMS of the random component. If we perform the MCMC analysis to fit for the B_{RMS} and f_{ord} parameters, we find that the latter is unaffected but the former is underestimated by approximately 7 per cent. We consider this acceptable given that our knowledge of the relative strengths of these components has not previously been anywhere near that accurate and that there are further limitations of our analysis discussed in § 6.

5.3 Non-linear parameters

Some of the parameters are fairly linearly related to the observables. The arm amplitudes, for example, simply increase the RM in a given direction, and since the RMs are the best dataset to use to constrain them, we use only the RM data to determine the a_n parameters (as seen in Fig. 7) as well as the angle ϕ_0 .

Parameters related to the synchrotron emission, particularly those describing the random magnetic field component, are more clearly non-linear. Firstly, the emission itself depends on the field to the power of γ as described in Eq. 1. Secondly, the observable polarised emission is affected by the random component much like a 2D random walk, whose mean distance from the starting point is then a function of the square root of the number of steps, N , and the step size. In the case of a power law GRF, we have essentially a superposition of random walks of many step sizes and N s.

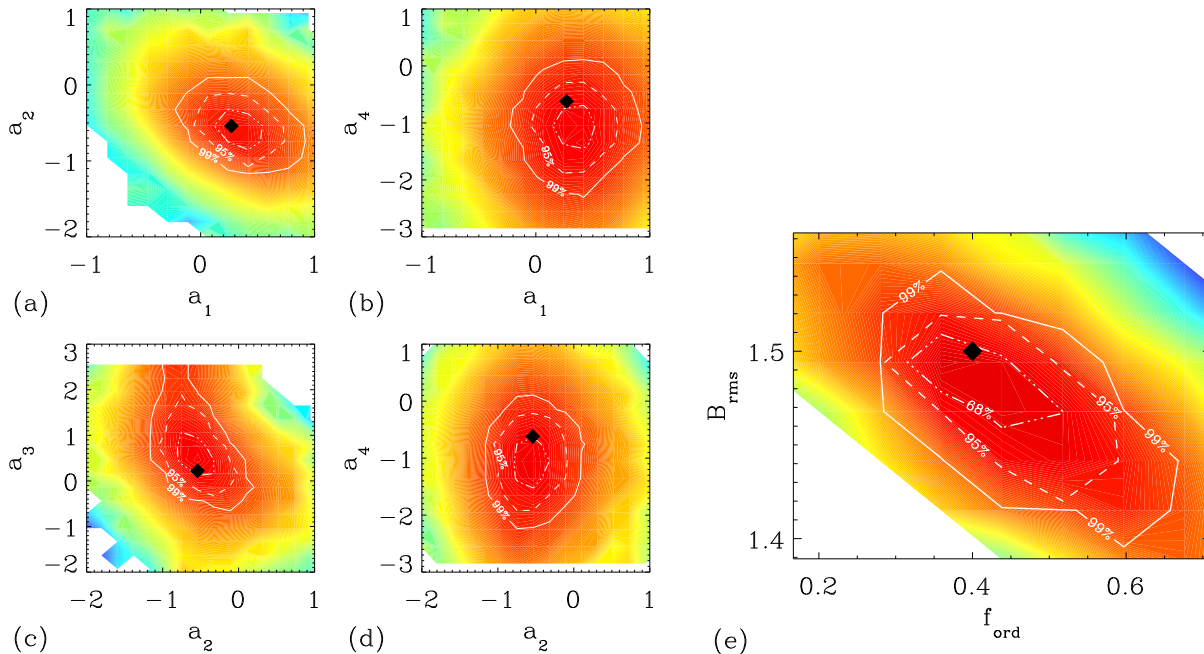


Figure 7. Example of MCMC results. The filled contours represent the mean likelihood showing the sampled region, while the white contour lines indicate the 68, 95, and 99.7 per cent confidence regions. The filled black diamonds give the correct input values. The examples on the *left*, (a) through (d), show the results for several of the six parameters describing the coherent magnetic field found fitting only to the RM data. On the *right* (e) are the results for the two parameters describing the amount of isotropic random and ordered components found using all the data.

Furthermore, the variance used in the likelihood calculation (Eq. 14) depends on the particular location in parameter space. As described above, this affects the “noise” due to the non-analytic way we compute the model. We have tested with a set of simulations to see how well the method works despite these shortcomings and found that it works surprisingly well. We fixed the other parameters and fit only to f_{ord} and B_{rms} , the two most important but perhaps most complicated and correlated parameters. Using both the total and polarised intensities does succeed in constraining these parameters. In all but one of the ten simulations, the resulting best-fit positions were within $2\text{-}\sigma$ of the correct values and showing no bias. An example is shown in Fig. 7.

6 RESULTS

Our principle aim is to attempt to constrain the ratios of the three components of the Galactic magnetic field: the coherent component, the isotropic random component, and the ordered component. With the three complementary datasets of total synchrotron emission, polarised synchrotron emission, and Faraday rotation measures, we have demonstrated that these three components can be disentangled using reasonable models of the magnetised ISM.

6.1 RM fits

We begin by constraining the large scale, coherent field. In other galaxies, the magnetic field usually shows spiral structure, sometimes azimuthally symmetric, sometimes not. We should not assume that the magnetic spiral follows the DIG

spiral; the field strength may or may not be higher in DIG arms, and even the spiral pitch angles may not be the same. But it is not our primary aim in this work to determine the global morphology of the coherent magnetic field. We use the RM data largely to *constrain* the amplitude of the emission due to the coherent field. Though its morphology may not follow precisely the spiral model we have fit to the data, it is enough to limit the amount of synchrotron emission from that component, allowing us to then examine that from the random and ordered components independently.

Using the methodology described in § 4, we fit a six parameter spiral model to the RM data alone to constrain the values of the following parameters: the orientation angle, ϕ_0 , the amplitudes a_0 to a_3 for each of the four arms, and a_4 for the “molecular ring”. The amplitudes a_n then give the relative strengths of each feature, which combine with C_0 to give the maximum field strength along the ridge. The relative amplitudes, particularly their signs that determine the direction of the field in each arm (clockwise or counterclockwise when viewed from the north Galactic pole) determine the features seen in the RM data as in Figs. 2 or 5.

The parameter fit results are shown in Table 2. This part of the analysis does not give much that is new compared to what has been done by Brown et al. (2007) and others. We do clearly see the magnetic field reversals, visible in the RM data, in the general direction of Scutum-Crux and near the tangent to the proposed “molecular ring” at negative longitudes. This is visible in comparing Figures 2 and 4. We also confirm the field strength peaking at $\approx 2\ \mu\text{G}$ in the arm ridges. It is interesting to note that, though the field is free to fit the azimuthal rotation ϕ_0 , the result lies very close

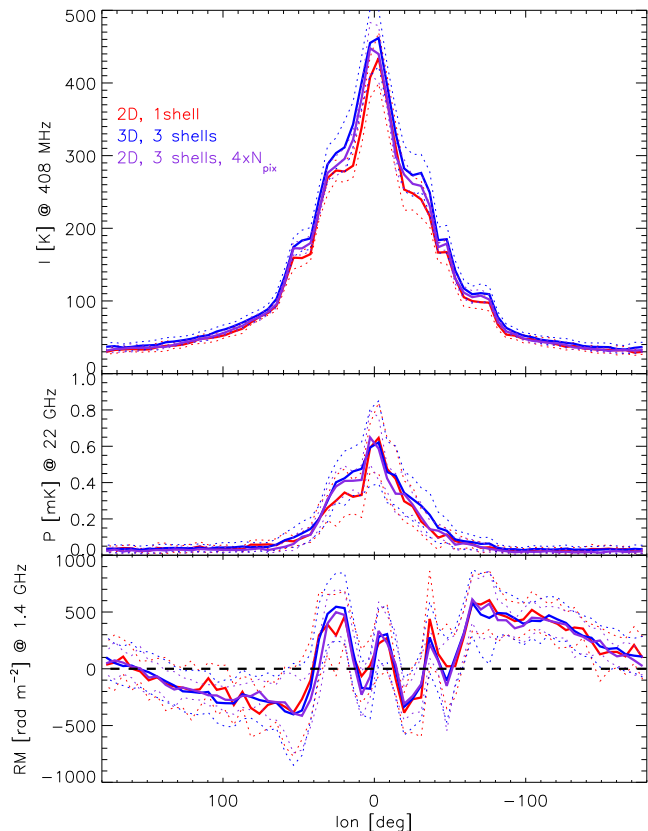


Figure 8. Testing the effects of resolution and dimension of GRF simulation as described in § 5.2. The solid lines are the mean models while the dotted lines indicate the RMS. The difference between our 2D analysis and a better but more time-consuming 3D method is apparent only in the strength of the step-features corresponding to spiral arm tangents where the small-scale random component is strongest. These differences are within the uncertainties but are systematic and introduce a small bias discussed in § 5.2.

to the DIG spiral arms in the NE2001 model, whether that model is assumed for the thermal electrons or not.

The value of a_0 is not constrained, because as seen in Fig. 4, no sightlines are really tangent to the arm. It contributes relatively little in the region where we have RM data.

6.2 Synchrotron fits

Our main aim, however, is to attempt to quantify the relative amounts of coherent, random, and ordered magnetic field components. As found by Broadbent et al., the magnetic field must be amplified in the arms. Since the cosmic rays are likely smooth on these scales, the step-like features in the synchrotron profile are probably due to the enhancement of the perpendicular component of the magnetic field in the arms. Though the coherent component could be scaled to produce such structures, it would also require an extremely low ($n_e \approx 10^{-3} \text{ cm}^{-3}$) electron density in order to be consistent with the RM data.

The fit results in Table 2 for the parameters B_{RMS} and f_{ord} are simply due to the relative strengths of the total and polarised emission along the plane. The resulting best-

fit profiles and residuals are shown in Fig. 10. These profiles are not a perfect match to the total intensity data, but they agree remarkably well in most places. The most significant deviation is where there is a strong thermal feature around longitude -70° to -80° , which is the region that dominates the high χ^2 . There is also a mismatch in the profile around longitude 60° which bears further investigating but appears to be related to the Sagittarius arm. Recall from § 2.1 that the innermost region is not included in the fit. Further work will be necessary to determine the magnetic field structure in the Galactic centre region; the model we use, particularly the central part of the profile shown in Fig. 3, is ill-constrained.

Figure 10 shows that the polarised synchrotron profiles are only fit to first order. The χ^2 values are not bad due to the galactic variance, but the residuals show clear systematic differences where the profile shape is wrong. More work will be needed to determine what this means for the model, particularly the spatial variation of the magnetic field components.

6.3 Component ratios

From the results of our fitting the parameters ϕ_0 , a_n , B_{rms} , and f_{ord} , we learn the following:

(i) The rotation measures allow us to constrain the coherent magnetic field parameters a_n . As shown in Fig. 5, they alone cannot distinguish between the NE2001 spiral model for the thermal electron density and a simple uniform model. Not shown on that figure are the synchrotron profiles, which are effectively indistinguishable. The reason is that the synchrotron profile is apparently dominated by the random and ordered components. The RMs, regardless of the thermal electron model, have constrained the coherent field to an amplitude that is fairly low compared to the synchrotron profile, assuming that the cosmic ray electron density is roughly correct.

Therefore, our results suggest that the coherent field in the arms peaks around $B_0 a_n (C_0 + 1) = 1 - 3 \mu\text{G}$ in the arms, varying from arm to arm with an average of $2 \mu\text{G}$.

(ii) The isotropic random field component peaks around $\langle B_{\text{iso}}^2 \rangle^{1/2} = (C_0 + 1) B_{\text{RMS}} = 4.2 \mu\text{G}$ (see Eq. 9).

(iii) The ordered field component peaks slightly lower at $3.3 \mu\text{G}$.

(iv) The fractions of the energy density in coherent, random, and ordered field components ($\propto \langle B^2 \rangle$) are then roughly 1:5:3, respectively. The uncertainties are discussed further in § 6.6. Note that this model implies a total *local* field strength of roughly $3 \mu\text{G}$, and a mean field strength in the inner 10 kpc of the Galaxy of $3.5 \mu\text{G}$.

6.4 Arm strength

In the basic analysis, the arm strengths, a_n , determine the coherent field strength in each arm (as well as direction) but do not affect the random or ordered components. For simplicity, these components are simply scaled by ρ_c as described in Table 1, which is only a function of the distance from the ridge. We can also, however, adjust the strength of these components by the same factors by multiplying C_0 by $|a_n|$. This makes the contrast in each arm proportional to

Fits to RM data only		
	NE2001	$n_e = 0.1 \text{ cm}^{-3}$
ϕ_0	70 ± 6.2	70 ± 7.8
a_0	1.65 ± 0.38	-0.15 ± 0.24
a_1	0.61 ± 0.18	0.33 ± 0.15
a_2	-1.04 ± 0.21	-0.87 ± 0.20
a_3	1.26 ± 0.64	0.97 ± 0.46
a_4	-1.00 ± 0.35	-1.33 ± 0.43
Fits to all data with above NE2001 n_e values fixed		
	constant compression	scaled
B_{RMS}	2.1 ± 0.03	2.1 ± 0.04
f_{ord}	1.9 ± 0.14	1.5 ± 0.16
χ^2_{I}/N	3.7	3.5
χ^2_{PI}/N	0.8	1.0
χ^2_{RM}/N	1.8	1.6

Table 2. *Top:* results of fitting RMs with the simple spiral model parameters and comparing constant thermal electron density model to NE2001. *Bottom:* results of fixing the ϕ_0 and a_n parameters to the best fit values show on top using NE2001 and all others to the “defaults” listed in Table 1, and then fitting only the f_{ord} and B_{RMS} parameters to all datasets. As described in § 6.4, the “constant compression” have the same amplitude of random components in each arm while the “scaled” have the factors of a_n applied.

the coherent field strength of that arm rather than constant. (It also implies that the ratio of the ordered to isotropic random fields changes from arm to arm.)

A comparison of the best-fit profiles is shown in Fig. 10. The physical motivation for scaling each arm strength independently is unclear, but the result including the extra scaling appears to fit the synchrotron profile slightly better in some places and slightly worse in others.

6.5 Arm/inter-arm Contrast

In the basic analysis presented above, we have fixed the value of the parameter C_0 that defines the contrast between the arm ridges and inter-arm regions. We can instead allow this parameter to vary as well. The combination of C_0 and B_{RMS} controls the relative strength of the arm versus the inter-arm region for the random component (as C_0 and B_0 or a_n does for the coherent component).

These three parameters, however, are somewhat degenerate as shown in Fig. 11. The data do not easily distinguish between a stronger B_{RMS} with a weaker contrast (C_0) or *vice versa*. This is an example of one of many degeneracies in the parameters listed in Table 1. But our basic result comparing the strengths of the components *in the arms* is not significantly affected.

6.6 Discussion

We have used the three complementary datasets of total synchrotron emission, polarised synchrotron emission, and rotation measure to study the three components of the Galactic magnetic field, namely the coherent, random, and ordered fields. We find that we can fit the profiles of these

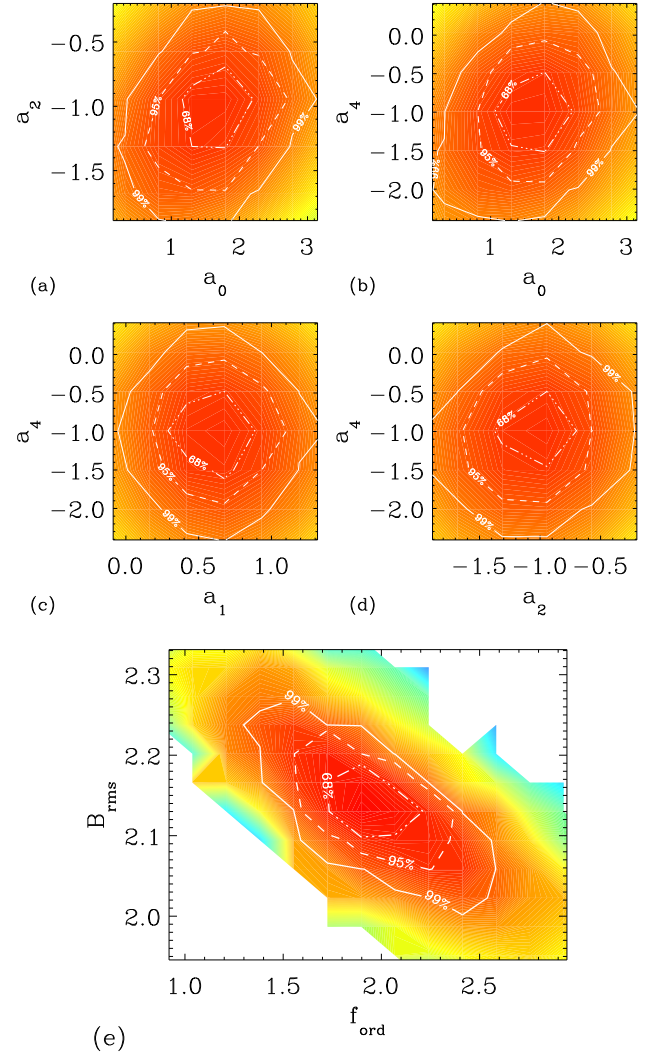


Figure 9. *Top, (a) through (d):* selected results of fitting the coherent field parameters to the RM data only using the NE2001 thermal electron density model. *Bottom, (e):* results of fixing the coherent field parameters to the values found in the RM analysis, and then fitting the two parameters controlling the small-scale, irregular components to all the data. The means and uncertainties are given in Table 2. Compare to Fig. 7.

datasets along the plane with a model where the components peak in magnetic arm ridges and where the coherent component contributes roughly 10 per cent to the energy density ($\langle B^2 \rangle$), while the random and ordered components contribute roughly 50 and 40 per cent, respectively.

This is a first attempt to constrain models with many parameters and degeneracies. If the estimates for the CRE and thermal electron densities are even approximately right, our method gives a fairly robust constraint on the *relative* strengths of the three field components. We should, however, quantify the impact of such assumptions and their uncertainties:

- There is a degeneracy between the thermal electron density in the arms and the amplitude of the coherent magnetic field. A factor of two uncertainty in the mean electron density in the arms implies a factor of two uncertainty in

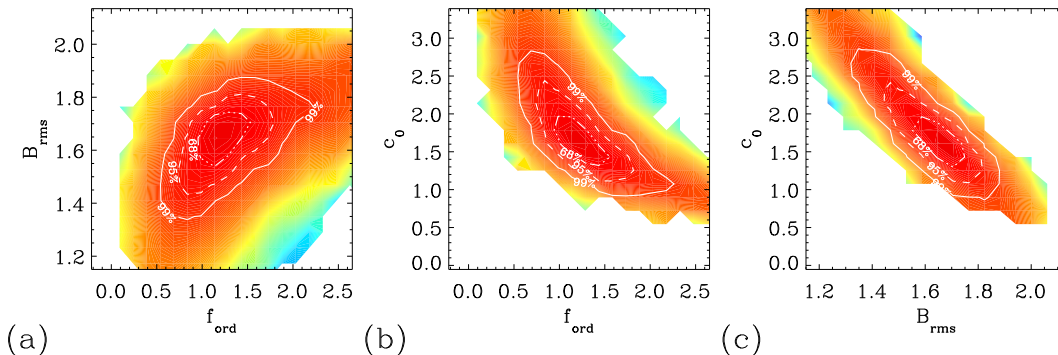


Figure 11. MCMC results showing the degeneracies described in § 6.5 among the three parameters: B_{RMS} , f_{ord} , and C_0 .

the coherent field strength. If the electron density is a factor of two smaller than our model for a given arm, the coherent field is then a factor of two larger to reproduce the same RM profile. This then requires a drop in B_{rms} to reproduce the same synchrotron total intensity profiles. The ratios of energy densities of the components (coherent:random:ordered) would go from roughly 1:5:3 to 6:3:1.

- Similarly, in using the NE2001 model for a smoothly distributed, average electron density, we have assumed a relatively homogeneous DIG, while clearly the density of free electrons varies many orders of magnitude from HII regions down to molecular clouds. Berkhuijsen et al. (2006) and others have studied its clumpiness as described by a filling factor. The LOS filling factor is often defined as $f \equiv \langle n_e^2 \rangle / \bar{n}_c^2$, where the brackets denote the average along the entire LOS while \bar{n}_c is the average value in the individual clumps; it then also represents the fraction of the LOS that falls within the clumps. This can also be defined as $f = \langle n_e \rangle^2 / \langle n_e^2 \rangle = DM^2 / (EMD)$ (where D is the total LOS distance, EM and DM are the emission and dispersion measures, respectively). We note that the factor derived from comparing EM and DM oversimplifies the fact that EM and DM essentially trace different physical components of the ISM.

The NE2001 is largely based on DM, which is linear in n_e and path length, and so any factor of $f \neq 1$ cancels. If the fluctuations in n_e are uncorrelated with the magnetic field, then RM is similarly unaffected on average. It is unclear how correlated the field is with the electron density, however, so the impact of this approximation is difficult to judge. If the field fluctuations along the LOS are equally likely to be toward or away from the observer in high density clumps, then even if the strength of the fluctuations is correlated with n_e , this will not affect the predicted mean RM profile, only its variance. If, however, the correlated field fluctuations retain a coherent direction, then the observed RM would be larger than what we have modelled. Properly taking this into account would then require a weaker field to reproduce the same RM data. In future, we may be able to plug in the results of magneto-hydrodynamic (MHD) turbulence simulations into the tools we have described to test this explicitly.

- There is a degeneracy between the magnetic field strength and the cosmic ray electron density. We assume a value of $J_{\text{CRE},\oplus} = 0.25 \text{ (GeV m}^2 \text{ sr)}^{-1}$ at the position of the Sun. If the uncertainty in this number is a factor of

two (which it may well be; see, e.g., Strong et al. 2004) and assuming B_{coh} is constrained by the RM data, then we can solve for the other components. The ratios of energy densities would then vary from 0.6:5:4 (CREs halved) to 3:5:2 (CREs doubled).

The recent results from the Fermi γ -ray telescope (Abdo et al. 2009) seem to indicate a density that is somewhat lower than what we use from Strong et al. (2007) based on EGRET data. A lower CRE density implies a larger random magnetic field component to reproduce the observed synchrotron emission. (The work of Sun et al. (2008) use an even higher density of $J_{\text{CRE},\oplus} = 0.4 \text{ (GeV m}^2 \text{ sr)}^{-1}$, which partly explains how they can reproduce roughly the observed amount of emission with only an isotropic random component and no ordered component.)

- We have assumed a spatially smooth cosmic-ray electron distribution with a simple power-law power spectrum that is the same throughout the Galaxy and has index $p = 3$. A spatial variation in the spectrum or deviations of the spectrum from the assumed power law would also affect our analysis.

As an example, we can imagine that the CRE spatial and spectral distribution varied between spiral arm and inter-arm regions due to the higher density of CRE acceleration sites (e.g., supernova remnants) in the arms (see, e.g., Case & Bhattacharya 1996). This would have a similar effect as the global uncertainty discussed above.

Furthermore, in assuming this power law distribution of electrons, we assume that the spectrum of synchrotron emission in brightness temperature also follows a power law with $\beta = -(p + 3)/2 = -3$. Analyses such as Platania et al. (1998) or Giardino et al. (2002) show that this index in fact varies across the sky. Determining this index on the plane over a broad frequency range is complicated by the variety of emission mechanisms that contribute to total intensity and by the Faraday effects that contribute to polarised intensity at low frequencies. If our assumption of $\beta = -3$ is too steep, our model will be underpredicting the polarised emission at 23 GHz from the coherent magnetic field component, for example. This is difficult to quantify, however, since both the synchrotron emissivity (as $B^{\frac{p+1}{2}}$) and the polarisation fraction ($\Pi = \frac{p+1}{p+7/3}$) depend on p .

- There are uncertainties in the zero-levels of the synchrotron datasets we used. These uncertainties are relatively small (e.g., a few K for the 408 MHz map), usually much less than the galactic variance, and will be most significant

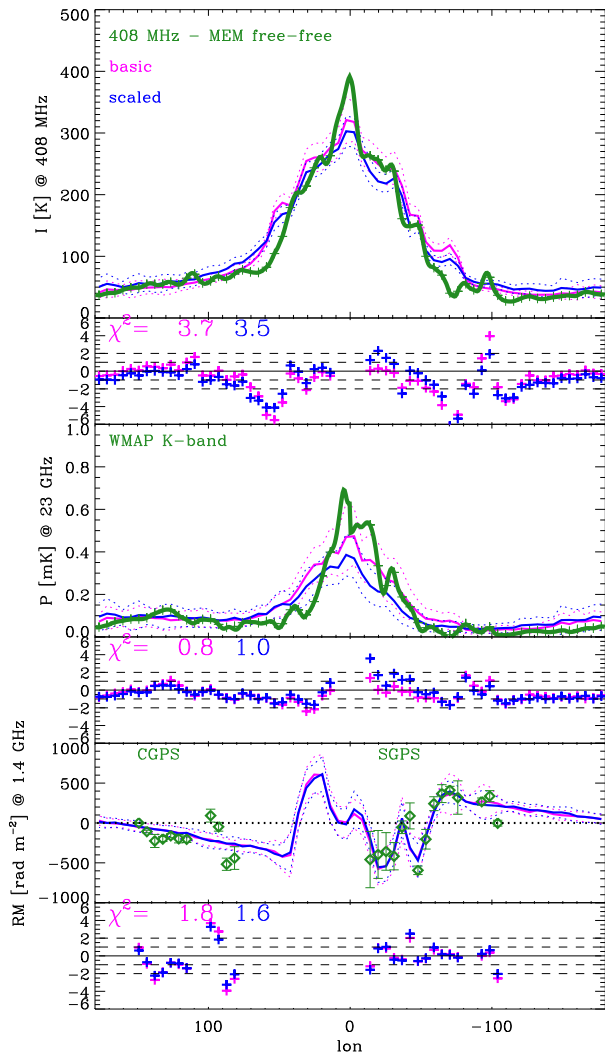


Figure 10. Best fit models from MCMC analysis as described in § 6.1 and 6.2. The three observables are shown from the top as synchrotron total intensity at 408 MHz, synchrotron polarised intensity at 23 GHz, and rotation measure. The solid blue and magenta lines are the mean models while the dotted lines indicate the RMS, or galactic variance, and in thick green are the data. For each observable, beneath the plotted profile are the residuals, i.e., $(data - model)/error$, compared to dashed lines at ± 1 and $\pm 2\sigma$. In magenta is the result where all arms have equal random and ordered compression, while in blue is the result where those components are also scaled by a_n as described in § 6.4.

where the synchrotron emission profile is lowest toward the Galactic anticentre. For our analysis of the magnetic field component ratios in the spiral arm peaks, this uncertainty is certainly not significant. It will, however, affect the parameters describing the strength of the field and the density of CREs in the outer region of the galaxy. As we have discussed above, these two distributions are degenerate and not constrained by our analysis. In future work, when we add dust emission to the analysis to break the degeneracy, we will also have to address the zero-levels more accurately. For this work, however, we consider the impact of the uncertainty minimal.

- We have assumed that the large-scale coherent field and

the small-scale field components are all strongest in the same regions, the magnetic spiral arm ridges. There is some evidence in one galaxy that the coherent field, in contrast to the random field, may be stronger in the inter-arm regions (Beck & Hoernes 1996). Further work will be needed to determine whether we can distinguish these possibilities.

Our results are the ratios of the field components’ energy densities that we measure as roughly 1:5:4 (coherent:random:ordered). The above uncertainties most significantly affect the fraction of magnetic field energy in the coherent component. The rough estimates above then imply that the coherent component could make up as little as 5 percent of the total energy in the field, or as much as 30 per cent given an uncertainty of a factor of 2 in the CRE density, or as much as 60 per cent if the thermal electrons are half the assumed value. The latter is certainly possible for a small region, but on the whole, pulsar distance measures averaged over the galaxy are unlikely to allow such a large discrepancy. As mentioned above, Fermi estimates of the CRE density are even lower than what we assumed, implying even larger random and ordered components.

There have been other efforts to estimate the amount of turbulence in the magnetic field. But one must be careful to understand what it is that is being measured, as these works generally distinguish only between a “regular” field and a “turbulent” field. Depending on the observable, what we define as the ordered field may count as either. Rand & Kulkarni (1989) and Ohno & Shibata (1993), for example, both look at RM data and measure a turbulent magnetic field component of $4 - 6 \mu\text{G}$ that corresponds to the sum of our ordered and isotropic random components. Schnitzeler et al. (2007) give an upper limit of $B_{\text{turb}}/B_{\text{reg},\perp} \approx 2$ based on synchrotron emission. Their “regular” component is, when only looking at synchrotron emission, the total of our coherent and ordered components. Haverkorn et al. (2004), by contrast, find a random component smaller than the “regular” component, though this is in two relatively small fields that may be probing smaller-scale structure only. Miville-Deschênes et al. (2008) find $B_{\text{turb}}/B_{\text{reg},\perp} = 0.57$ using synchrotron polarisation in *WMAP* data, so again, the “regular” component includes what we define as ordered. Each of these studies uses different observables, different regions of the Galaxy, and different assumptions. It is thus difficult to compare their results with each other or with our estimate, but with the exception of the Haverkorn et al. result, they are roughly consistent.

What we can conclude, however, is that the coherent field is likely a relatively small fraction of the total and that a model including only an isotropic random component and a coherent field is incomplete. To reproduce all of the observables, particularly the polarised emission, requires an ordered field component as well.

7 CONCLUSIONS

We have outlined a method to simulate observables such as synchrotron emission and Faraday rotation measure based on parametrised models of the physical components of the Galaxy and to use these to study the complicated parameter space in an MCMC analysis. In particular, we describe how to deal with the galactic variance due to the fact that one of

the principle physical components is stochastic. These tools can be used to model the global properties of the Galaxy's magnetic field in 3D or to study the turbulent component of the magneto-ionic medium in detail without the need for as many simplifying assumptions.

To demonstrate the method's utility, we have used the three complementary datasets of total synchrotron emission, polarised synchrotron emission, and rotation measure to try to constrain the relative contributions of the coherent, random, and ordered components of the magnetic field. We find the relative energy densities of these components to be roughly 1:5:3, respectively, at their peaks in a magnetic spiral arm model. If our assumed CRE and thermal electron distributions are roughly correct, then this implies arm field strengths of 2, 4, and 3 μG , respectively. This particular analysis is limited by several simplifying assumptions, but we consider the result a first step and proof-of-concept showing how to tackle this complicated problem.

In future work, we will address some of the limitations and degeneracies discussed above. More importantly, we look forward to the prospect of additional data. In the next few years, we will have the C-Band All Sky Survey (C-BASS)⁴ at 5 GHz giving a much more sensitive measurement of the polarised synchrotron emission in the radio bands. These data will help us to study the spectral variation of the synchrotron emission, and in turn the distribution of cosmic ray electrons.

The Planck satellite (The Planck Collaboration 2006) will also provide a higher sensitivity polarised synchrotron sky map in the microwave bands when combined with continuing observations by *WMAP*. Its many bands will also contribute, along with C-BASS and *WMAP*, to a much more accurate separation of the thermal emission than is currently possible. This will improve our fitting of the step features in the synchrotron emission along the plane where the thermal emission is a problem. Furthermore, the High Frequency Instrument on Planck will give us a much better map of the polarised dust emission, a completely independent tracer of the magnetic fields that we have not used in this work.

The GALFACTS⁵ survey at Arecibo Observatory will give us the vital coverage of the northern side of the Galactic centre in rotation measures (see Fig. 2). This will be crucial in distinguishing the various models of the magnetic field reversals currently so controversial. And that in turn will inform theories such as dynamo models for the origin, amplification, and evolution of the coherent field.

The Australian Square Kilometre Array Pathfinder (ASKAP)⁶ will significantly improve our southern sky coverage of rotation measures. Even better will be the Square Kilometre Array⁷ itself. Johnston & et al. (2008) and Gaensler et al. (2004) describe how these will significantly advance magnetic field studies. Not only will they inform our knowledge of our own galaxy but allow us to make similar observations of external galaxies using background polarised sources.

ACKNOWLEDGEMENTS

The authors would like to thank A. Strong and C. Dickinson for useful discussions. We acknowledge use of the HEALPix software (Górski et al. 2005) for some of the results in this work. We acknowledge the use of the Legacy Archive for Microwave Background Data Analysis (LAMBDA). Support for LAMBDA is provided by the NASA Office of Space Science.

REFERENCES

- Abdo A. A., Ackermann M., Ajello M., Atwood W. B., Axelsson M., Baldini L., Ballet J., Barbiellini G., Bastieri D., Battelino M., Baughman B. M., Bechtol K., Bellazzini 2009, PRD, 102, 181101
- Beck R., 2009, Proc. IAU Symposium, 259, pp 3–14
- Beck R., Hoernes P., 1996, Nature, 379, 47
- Berkhuijsen E. M., Mitra D., Mueller P., 2006, Astronomische Nachrichten, 327, 82
- Beuermann K., Kanbach G., Berkhuijsen E. M., 1985, AAP, 153, 17
- Broadbent A., 1989, (PhD thesis, Durham Univ.)
- Broadbent A., Haslam T. C. G., Osborne L. J., 1990, International Cosmic Ray Conference, 3, 229
- Brown J. C., Haverkorn M., Gaensler B. M., Taylor A. R., Bizunok N. S., McClure-Griffiths N. M., Dickey J. M., Green A. J., 2007, ApJ, 663, 258
- Brown J. C., Taylor A. R., Jackel B. J., 2003, ApJS, 145, 213
- Burn B. J., 1966, MNRAS, 133, 67
- Case G., Bhattacharya D., 1996, A&AS, 120, C437+
- Cordes J. M., Lazio T. J. W., 2002, preprint (astro-ph/0207156)
- de Oliveira-Costa A., Tegmark M., Gaensler B. M., Jonas J., Landecker T. L., Reich P., 2008, MNRAS, 388, 247
- Dick J., Knox L., Chu M., 2006, Journal of Cosmology and Astro-Particle Physics, 7, 1
- Dickinson C., Davies R. D., Davis R. J., 2003, MNRAS, 341, 369
- Drimmel R., Spergel D. N., 2001, ApJ, 556, 181
- Finkbeiner D. P., 2004, ApJ, 614, 186
- Gaensler B. M., Beck R., Feretti L., 2004, New Astronomy Review, 48, 1003
- Giardino G., Banday A. J., Górski K. M., Bennett K., Jonas J. L., Tauber J., 2002, AAP, 387, 82
- Gold B., Bennett C. L., Hill R. S., Hinshaw G., Odegard N., Page L., Spergel D. N., Weiland J. L., Dunkley J., Halpern M., Jarosik N., Kogut A., Komatsu E., Larson D., Meyer S. S., Nolte M. R., Wollack E., Wright E. L., 2009, ApJS, 180, 265
- Górski K. M., Hivon E., Banday A. J., Wandelt B. D., Hansen F. K., Reinecke M., Bartelmann M., 2005, ApJ, 622, 759
- Han J. L., Ferriere K., Manchester R. N., 2004, ApJ, 610, 820
- Han J. L., Manchester R. N., Lyne A. G., Qiao G. J., van Straten W., 2006, ApJ, 642, 868
- Han J. L., Qiao G. J., 1994, AAP, 288, 759
- Haslam C. G. T., Stoffel H., Salter C. J., Wilson W. E., 1982, A&AS, 47, 1

⁴ <http://www.astro.caltech.edu/cbass/>

⁵ <http://www.ucalgary.ca/ras/GALFACTS/>

⁶ <http://www.atnf.csiro.au/projects/askap/>

⁷ <http://www.skatelescope.org/>

- Haverkorn M., Katgert P., de Bruyn A. G., 2004, AAP, 427, 169
- Heiles C., 1996, ApJ, 462, 316
- Hinshaw G., Nolte M. R., Bennett C. L., Bean R., Doré O., Greason M. R., Halpern M., Hill R. S., Jarosik N., Kogut A., 2007, ApJS, 170, 288
- Hinshaw G. e. a., 2009, ApJS, 180, 225
- Jansson R., Farrar G. R., Waelkens A. H., Enßlin T. A., 2009, Journal of Cosmology and Astro-Particle Physics, 7, 21
- Johnston S., et al. 2008, Experimental Astronomy, 22, 151
- Jonas J. L., Baart E. E., Nicolson G. D., 1998, MNRAS, 297, 977
- Lewis A., Bridle S., 2002, PRD, 66, 103511
- Mills B. Y., 1959, in Bracewell R. N., ed., URSI Symp. 1: Paris Symposium on Radio Astronomy Vol. 9 of IAU Symposium, Galactic structure at meter wavelengths. pp 431–+
- Miville-Deschênes M.-A., Ysard N., Lavabre A., Ponthieu N., Macías-Pérez J. F., Aumont J., Bernard J. P., 2008, AAP, 490, 1093
- Ohno H., Shibata S., 1993, MNRAS, 262, 953
- Orlando E., Strong A. W., Moskalenko I. V., Porter T. A., Johannesson G., Digel S. W., 2009, preprint (arXiv:0907.0553)
- Page L., Hinshaw G., Komatsu E., Nolte M. R., Spergel D. N., Bennett C. L., Barnes C., Bean R., Doré O., Dunkley J., Halpern M., 2007, ApJS, 170, 335
- Platania P., Bensadoun M., Bersanelli M., de Amici G., Kogut A., Levin S., Maino D., Smoot G. F., 1998, ApJ, 505, 473
- Rand R. J., Kulkarni S. R., 1989, ApJ, 343, 760
- Reich P., Reich W., 1986, A&AS, 63, 205
- Reich W., 1982, A&AS, 48, 219
- Rybicki G. B., Lightman A. P., 1979, Radiative processes in astrophysics. Wiley-Interscience, New York
- Schnitzeler D. H. F. M., Katgert P., de Bruyn A. G., 2007, AAP, 471, L21
- Strong A. W., Moskalenko I. V., Ptuskin V. S., 2007, Annual Review of Nuclear and Particle Science, 57, 285
- Strong A. W., Moskalenko I. V., Reimer O., 2004, ApJ, 613, 962
- Sun X. H., Reich W., Waelkens A., Enßlin T. A., 2008, AAP, 477, 573
- The Planck Collaboration 2006, (astro-ph/0604069)
- Waelkens A., Jaffe T., Reinecke M., Kitaura F. S., Enßlin T. A., 2009, AAP, 495, 697

This paper has been typeset from a $\text{\TeX}/\text{\LaTeX}$ file prepared by the author.